

Two-photon photoassociation of hot magnesium atoms by femtosecond pulses: A quantum dynamical study

Saieswari Amaran and Ronnie Kosloff

Fritz Haber Research Centre and The Department of Physical Chemistry, Hebrew University, Jerusalem 91904, Israel

Michał Tomza and Robert Moszynski

Department of Chemistry, University of Warsaw, Pasteura 1, 02-093 Warsaw, Poland

Leonid Rybak, Liat Levin, and Zohar Amitay

The Shirlee Jacobs Femtosecond Laser Research Laboratory, Schulich Faculty of Chemistry, Technion-Israel Institute of Technology, Haifa 32000, Israel

Christiane P. Koch

Institut für Theoretische Physik, Freie Universität Berlin, Arnimallee 14, 14195 Berlin, Germany and

Theoretische Physik, Universität Kassel, Heinrich-Plett-Straße 40, 34132 Kassel, Germany^{a)}

Two-photon photoassociation of hot magnesium atoms by femtosecond laser pulses is studied from first principles, combining *ab initio* quantum chemistry and molecular quantum dynamics. This theoretical framework allows for rationalizing the generation of molecular rovibrational coherence from thermally hot atoms [L. Rybak *et al.*, Phys. Rev. Lett. **107**, 273001 (2011), arXiv:1107.4755]. The coupled cluster and multi-reference configuration interaction frameworks are used to calculate the relevant potential energy curves, one-photon and two-photon transition matrix elements, dynamical Stark shifts, as well as spin-orbit couplings and non-adiabatic radial couplings. Random phase thermal wavefunctions are employed to model the thermal ensemble of hot colliding atoms. Comparing three different choices of random phase thermal wavefunctions, the free propagation approach is found to have the fastest initial convergence for the photoassociation yield. When further refinement is required the eigenvalue approach is superior. The interaction of the colliding atoms with two time-delayed femtosecond laser pulses is modeled non-perturbatively to account for strong-field effects observed in the experiment. Good agreement between experimental and theoretical results is obtained.

I. INTRODUCTION

Molecules can be assembled from atoms using laser light. This process is termed photoassociation. With the advent of femtosecond lasers and pulse shaping techniques, photoassociation became a natural candidate for coherent control of a binary reaction. Coherent control had been conceived as a method to determine the fate of chemical reactions using laser fields.¹ The basic idea is to employ interference of matter waves to constructively enhance a desired outcome while destructively suppressing all undesired alternatives.^{2,3} Control is exerted by shaping the laser pulses, the simplest control knobs being time delays and phase differences.⁴ Over the last two decades, the field of coherent control has developed significantly both theoretically and experimentally.^{5–9} However, a critical examination of the achievements reveals that successful control has been demonstrated almost exclusively for unimolecular processes such as ionization, dissociation and fragmentation. It is natural to ask why the reverse process of controlling binary reactions^{10–18} is so much more difficult.

The main difference between unimolecular processes and a binary reaction lies in the initial state – a single or

few well-defined bound quantum states vs an incoherent continuum of scattering states.¹⁹ For a binary reaction, the nature of the scattering continuum is mainly determined by the temperature of the reactants. As temperature decreases, higher partial waves are frozen out. At the very low temperatures of ultracold gases, the scattering energy of atom pairs is so low that the rotational barrier cannot be passed, and the scattering becomes purely *s*-wave.²⁰ In this regime, the reactants are pre-correlated due to quantum threshold effects²¹ and the effect of scattering resonances is particularly pronounced.^{22–24} At a temperature of about 100 μ K, photoassociation with femtosecond laser pulses has been demonstrated.²⁵ Coherent transient Rabi oscillations were observed as the prominent feature in the pump-probe spectra. The transients are due to long tails of the pulses caused by a sharp spectral cut which is necessary to avoid excitation into unbound states.^{25,26} This pinpoints to the fact that the large spectral bandwidth of a femtosecond pulse is not well adapted to one-photon photoassociation at ultralow temperatures which requires narrow-band excitation.²⁷

The situation changes completely for high temperatures where the scattering states can penetrate rotational barriers due to the large translational kinetic energy. The association process is then likely to happen at short internuclear distance close to the inner turning point and for highly excited rotational states. In this case, the large spectral bandwidth of femtosecond laser pulses is

^{a)} Electronic mail: christiane.koch@uni-kassel.de

ideally adapted to both the broad thermal width of the ensemble of scattering states and the depth of the electronically excited state potential in which molecules are formed. The disadvantage of this setting is that the initial state is completely incoherent, impeding control of the photoreaction. Photoassociation with femtosecond laser pulses was first demonstrated under these conditions, employing a one-photon transition in the UV.¹⁰ Subsequent to the photoassociation, coherent rotational motion of the molecules was observed.¹⁰ We have recently demonstrated generation of both rotational and vibrational coherences by two-photon femtosecond photoassociation of hot atoms.^{28,29} This is a crucial step toward the coherent control of photoinduced binary reactions since the fate of bond making and breaking is determined by the vibrational motion.

Employing multi-photon transitions comes with several advantages: The class of molecules that can be photoassociated by near-IR/visible femtosecond laser pulses is significantly larger for multi-photon transitions compared to one-photon excitation. Femtosecond laser technology is most advanced in the near-IR spectral region. Due to the different selection rules, different electronic states become accessible for multi-photon transitions compared to one-photon excitation. Control strategies differ for multi-photon and one-photon excitation. In particular, large dynamic Stark shifts and an extended manifold of quantum pathways that can be interfered come into play for multi-photon excitation.³⁰ The theoretical description needs to account for these strong-field effects.

We have constructed a comprehensive theoretical model from first principles to describe the experiment in which magnesium atoms in a heated cell are photoassociated by femtosecond laser pulses.^{28,29} It is summarized in Figure 1. Magnesium in its electronic ground state is a closed shell atom. Its ground electronic potential, $X^1\Sigma_g^+$, therefore displays only a weak van der Waals attractive well. A femtosecond pulse of 100 fs transform-limited duration with a central wavelength of ~ 840 nm promotes an electron to the π orbital. This two-photon transition is driven since a wavelength of 840 nm is far from any one-photon resonance both for magnesium atoms and Mg_2 molecules, cf. Fig. 1. Upon excitation, a strong chemical bond is formed in the $(1)^1\Pi_g$ state with a binding energy of ~ 1.8 eV or, equivalently, ~ 14500 cm^{-1} . A time-delayed femtosecond pulse probes the excited Mg_2 molecule by inducing a one-photon transition to a higher excited electronic state ($^1\Pi_u$). This state has a strong one-photon transition back to the ground state. The corresponding experimental observable is the intensity of the resulting UV fluorescence (~ 290 nm), measured as a function of the pump-probe time delay. An oscillating signal is a manifestation of coherent rovibrational dynamics in the $^1\Pi_g$ state.^{28,29}

The correct description of the thermal initial state is crucial to capture the generation of coherence out of an incoherent ensemble. The density operator, $\hat{\rho}_T$, describ-

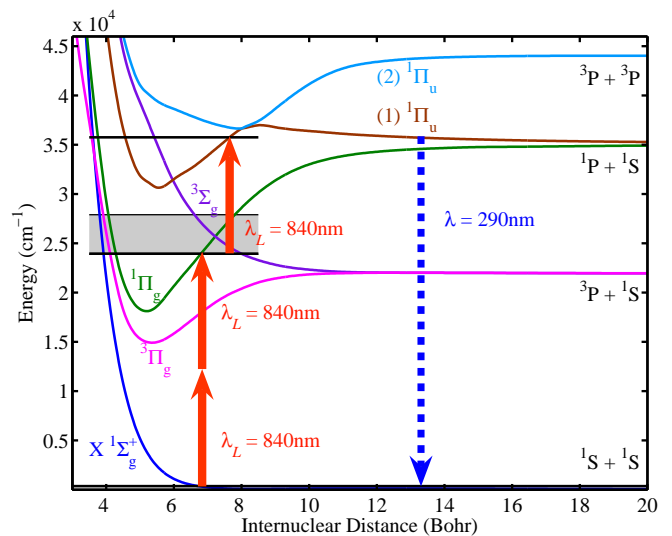


FIG. 1. Potential energy curves of the electronic states involved in the two-photon photoassociation probed by a time-delayed pulse. The shaded region indicates the vibrational band populated after photoassociation.

ing the initial state of hot atom pairs at temperature, T , is constructed by a thermal average over suitable basis functions. Since no dissipative processes occur on the sub-picosecond timescale of the experiment, the coherent time evolution of the density operator is most easily carried out by propagating the basis functions. Expectation values are obtained by thermally averaging the corresponding operator over the propagated basis functions. A numerically efficient description of the initial thermal ensemble is thus essential to facilitate the time-dependent simulations. This is the main subject of our present work.

The paper is organized as follows. Section II identifies the relevant electronic states and presents their potential energy curves, transition matrix elements and non-adiabatic couplings. These are obtained employing highly accurate state of the art *ab initio* methods. An effective description of the thermal ensemble of translationally and rotationally hot atom pairs in their electronic ground state based on random phase thermal wavepackets is developed in Section III. Three different choices of basis functions are discussed. Section IV introduces the light-matter interaction. The time-dependent Schrödinger equation is solved separately for the pump and probe pulses. Convergence of the photoassociation probability is studied in Section V for the different thermal averaging procedures, and the role of shape resonances is discussed. Section VI investigates the generation of coherence in terms of the quantum purity and a dynamical coherence measure. Finally, we conclude in Section VII.

II. AB INITIO POTENTIAL ENERGY CURVES, TRANSITION DIPOLE MOMENTS, AND NONADIABATIC COUPLING MATRIX ELEMENTS

State-of-the-art *ab initio* techniques have been applied to compute the potential energy curves of the magnesium dimer in the Born-Oppenheimer approximation. In all calculations the aug-cc-pVQZ basis set of quadruple zeta quality as the atomic basis for Mg were used. In addition, this basis set was augmented by the set of bond functions consisting of $[3s3p2d2f1g1h]$ functions placed in the middle of the Mg_2 dimer bond. All potential energy curves were obtained by a supermolecule method and the Boys and Bernardi scheme was used to correct for the basis-set superposition error.³¹

The ground $X^1\Sigma_g^+$ state potential was computed with the coupled cluster method restricted to single, double, and noniterative triple excitations, CCSD(T). For the excited $^1\Pi_g$ and $(1)^1\Pi_u$ states we used the linear response theory (equation of motion approach) within the coupled-cluster singles and doubles framework, LRCCSD. The potential energy curve of the excited $(2)^1\Pi_u$ state in the region of the minimum of the potential was also obtained with the LRCCSD method, whereas at larger internuclear distances this potential energy curve was represented by the multipole expansion with electrostatic and dispersion terms C_n/R^n up to and including $n = 10$. The long-range coefficients C_n were obtained within the multireference configuration interaction method restricted to single and double excitations, MRCI, with a large active space. The latter procedure was necessary since the $(2)^1\Pi_u$ state dissociates into $\text{Mg}(^3\text{P})+\text{Mg}(^3\text{P})$ atoms and cannot be asymptotically described by a single Slater determinant. The energy of the separated atoms was set equal to the experimental value for each electronic state, although the atomic excitation energies obtained from the LRCCSD calculations were very accurate and for the lowest ^1P state the deviation from the experimental values was approximately 100 cm^{-1} .

A high accuracy of the computed potential energy curves is confirmed by an excellent agreement of the theoretical dissociation energy for the ground $X^1\Sigma_g^+$ state ($D_0 = 403.1\text{ cm}^{-1}$) with the experimental value ($D_0 = 404.1 \pm 0.5\text{ cm}^{-1}$).³² Moreover, the number of bound vibrational states for $J = 0$ supported by the electronic ground state agrees with the experimental number $N_\nu = 19$. Spectroscopic parameters of another experimentally observed state, $A^1\Sigma_u^+$, also agree with our values, for the well position within 0.07 Bohr , while the binding energy ($D_e = 9427\text{ cm}^{-1}$) is only 0.4% higher than the experimental value ($D_e = 9387\text{ cm}^{-1}$).³² Also the root mean square deviation of the rovibrational levels computed with the potential energy curves from the CCSD(T) and LRCCSD calculations for the ground and A states were 1.3 cm^{-1} and 30 cm^{-1} , respectively, i.e. 0.3% of the potential well depth. Such a good agreement of the calculations with the available experimental data strongly suggests that we can expect a comparable level

of accuracy for other computed potential energy curves and molecular properties. More details on the *ab initio* calculations and spectroscopic characteristics of various electronic states of Mg_2 will be reported elsewhere.³³

The electric transition dipole moments between states i and f $\mu_i = \langle \Psi_i | \hat{\mu}_i | \Psi_f \rangle$ where the electric dipole operator $\hat{\mu}_i = r_i$ is given by the i th component of the position vector and $\Psi_{i/f}$ are the wave functions for the initial and final states, respectively, were computed as the first residue of the LRCCSD linear response function for $X^1\Sigma_g^+$, $^1\Pi_g$, and $^1\Pi_u(1)$ states, whereas for transitions to $(2)^1\Pi_u$ state MRCI method was applied.

Nonadiabatic radial and angular coupling matrix elements, as well as the spin-orbit coupling matrix elements have been evaluated with the MRCI method. The adiabatic $(1)^1\Pi_u$ and $(2)^1\Pi_u$ states are strongly coupled by the nuclear momentum operator $\hat{\mathbf{T}}_R = i\nabla_R/\mu$. Therefore to include this non-adiabatic coupling in the model one has to switch to the diabatic representation, i.e. to using diabatic potential energy curves and coupling potentials:

$$\mathbf{V}(R) = \begin{pmatrix} V_{11}^d(R) & V_{12}(R) \\ V_{21}(R) & V_{22}^d(R) \end{pmatrix} \quad (1)$$

where V_{11}^d and V_{22}^d are the diagonal diabatic potentials, while $V_{12}(R) = V_{21}(R)$ is the coupling term. The potential curves corresponding to the diabatic potentials V_{11}^d and V_{22}^d may cross, and are obtained from the following expression,

$$\mathbf{V}(R) = \mathbf{A}^{-1}(R) \begin{pmatrix} V_{(1)^1\Pi_u}(R) & 0 \\ 0 & V_{(2)^1\Pi_u}(R) \end{pmatrix} \mathbf{A}(R), \quad (2)$$

where $V_{(1/2)^1\Pi_u}(R)$ are the adiabatic potential energy curves for the $(1)^1\Pi_u$ and $(2)^1\Pi_u$ states, and the matrix $\mathbf{A}(R)$ takes the form

$$\mathbf{A}(R) = \begin{pmatrix} \cos \zeta(R) & \sin \zeta(R) \\ -\sin \zeta(R) & \cos \zeta(R) \end{pmatrix}, \quad (3)$$

where

$$\zeta(R) = \int_R^\infty \tau(R') dR'. \quad (4)$$

The nonadiabatic radial coupling $\tau(R)$ is given by:

$$\tau(R) = \left\langle \Psi_{(1)^1\Pi_u} \left| \frac{d}{dR} \right| \Psi_{(2)^1\Pi_u} \right\rangle. \quad (5)$$

Diabatic molecular wave functions Ψ_d are constructed from the adiabatic ones by applying the transformation

$$\begin{pmatrix} \Psi_{d1} \\ \Psi_{d2} \end{pmatrix} = \mathbf{A}(R) \begin{pmatrix} \Psi_{(1)^1\Pi_u} \\ \Psi_{(2)^1\Pi_u} \end{pmatrix}, \quad (6)$$

so the corresponding transition moments from the state i to the diabatic states can be obtained from those in the adiabatic basis

$$\begin{pmatrix} \langle \Psi_i | \hat{X} | \Psi_{d1} \rangle \\ \langle \Psi_i | \hat{X} | \Psi_{d2} \rangle \end{pmatrix} = \mathbf{A}(R) \begin{pmatrix} \langle \Psi_i | \hat{X} | \Psi_{(1)^1\Pi_u} \rangle \\ \langle \Psi_i | \hat{X} | \Psi_{(2)^1\Pi_u} \rangle \end{pmatrix}. \quad (7)$$

Weak spin-orbit coupling between the $(1)^1\Pi_g$, $(1)^3\Pi_g$, and $(1)^3\Sigma_g$ states was also taken into account in our dynamical model. The spin-orbit matrix elements relevant for our work read:

$$W_1(R) = \langle \Psi_{(1)^1\Pi_g} | H_{\text{SO}} | \Psi_{(1)^3\Sigma_g} \rangle, \quad (8)$$

$$W_2(R) = \langle \Psi_{(1)^1\Pi_g} | H_{\text{SO}} | \Psi_{(1)^3\Pi_g} \rangle, \quad (9)$$

$$W_3(R) = \langle \Psi_{(3)^1\Pi_g} | H_{\text{SO}} | \Psi_{(1)^3\Sigma_g} \rangle, \quad (10)$$

where H_{SO} the spin-orbit coupling Hamiltonian in the Breit-Pauli approximation including all one- and two-electron terms. The spin-orbit coupling matrix elements were computed with the multireference configuration interaction method restricted to single and double excitations (MRCI).

The two-photon electric dipole coupling,

$$\chi(\omega_L, t, R) = \frac{1}{4} |S(t)|^2 \sum_{i,j} E_i E_j M_{ij}^{f \leftarrow 0}(\omega_L, R), \quad (11)$$

is given by the tensor elements of the two-photon electric transition dipole moment between the ground 0 and excited f state,

$$M_{ij}^{f \leftarrow 0}(\omega_L, R) = - \sum_{n \neq 0} \left[\frac{\langle f | \hat{\mu}_i | n \rangle \langle n | \hat{\mu}_j | 0 \rangle}{\omega_{n0} - \omega_L} + \frac{\langle f | \hat{\mu}_j | n \rangle \langle n | \hat{\mu}_i | 0 \rangle}{\omega_{nf} + \omega_L} \right] \quad (12)$$

where $\omega_L = hc/\lambda_L$. In practice, the two-photon transition moment given by the expression above can be obtained as a residue of the cubic response function.³⁴ For transitions between the $X^1\Sigma_g^+$ and $^1\Pi_g$ states, $M_{ij}^{f \leftarrow 0}(\omega_L, R)$ was computed as a residue of the coupled cluster cubic response function with electric dipole operators and wave functions within the CCSD framework.^{35,36}

The Stark shift of k state can be expressed in terms of the elements of the dynamic electric dipole polarizability tensor,

$$\omega_k^S(\omega_L, t, R) = -\frac{1}{4} |S(t)|^2 \sum_{i,j} E_i E_j \alpha_{ij}^k(\omega_L, R), \quad (13)$$

where the tensor elements of the dynamic polarizability are given by

$$\alpha_{ij}^k(\omega_L, R) = \sum_{n \neq k} \left[\frac{\langle k | \hat{\mu}_i | n \rangle \langle n | \hat{\mu}_j | k \rangle}{\omega_{nk} - \omega_L} + \frac{\langle k | \hat{\mu}_j | n \rangle \langle n | \hat{\mu}_i | k \rangle}{\omega_{nk} + \omega_L} \right]. \quad (14)$$

The tensor elements of the electric dipole polarizability of the ground $X^1\Sigma_g^+$ state were obtained as the coupled cluster linear response function with electric dipole operators and wave functions within CCSD framework.³⁷ Dynamic polarizabilities of the excited states were computed as double residues of the coupled cluster cubic response function with electric dipole operators and wave functions within CCSD framework.^{38,39}

The CCSD(T) and CCSD calculations (including response functions calculations) were performed with the DALTON program,⁴⁰ while MRCI calculations were done with the MOLPRO suite of codes.⁴¹

III. QUANTUM DYNAMICAL DESCRIPTION OF A THERMAL ENSEMBLE

The initial state for photoassociation is given by the ensemble of magnesium atoms in the heated cell which interact via the $X^1\Sigma_g^+$ electronic ground state potential. Assuming equilibrium, the initial state is represented by the canonical density operator for N atoms held in a volume V at temperature T . Due to the moderate density in a heat pipe, the description can be restricted to atom pairs. The density operator for $N/2$ atom pairs is then obtained from that for a single atom pair,⁴² $\hat{\rho}_T(t=0)$, which is expanded into a suitable complete orthonormal basis. Thermally averaged time-dependent expectation values of an observable $\hat{\mathbf{A}}$ are calculated according to

$$\langle A(t) \rangle_T = \text{Tr}[\hat{\mathbf{A}} \hat{\rho}_T(t)]. \quad (15)$$

with the time evolution of $\hat{\rho}_T(t)$ given by $\hat{\rho}_T(t) = \hat{\mathbf{U}}(t, 0) \hat{\rho}_T(t=0) \hat{\mathbf{U}}^\dagger(t, 0)$ starting from the initial state

$$\hat{\rho}_T(t=0) = \frac{1}{Z} e^{-\beta \hat{\mathbf{H}}},$$

where $\beta = 1/k_B T$ and $Z = \text{Tr}[e^{-\beta \hat{\mathbf{H}}}]$ the partition function (since we are not interested in calculating absolute numbers, normalization by Z will be omitted below). For a thermal, i.e. incoherent, initial state, undergoing coherent time evolution, the dynamics can be captured by solving the Schrödinger equation for each basis function. Solving the Liouville von-Neumann equation for the density operator is not necessary if dissipation can be neglected on the timescales considered. Thermally averaged expectation values are then calculated by properly summing over the expectation values obtained from the propagated basis states.⁴²

Since many scattering states in a broad distribution of rotational quantum numbers are thermally populated, the approach of propagating all thermally populated basis states directly⁴² becomes numerically expensive. Instead, an effective description of the thermal ensemble of scattering atoms is obtained by implementing thermal averaging as an average over realizations of random phases. It makes use of thermal random wavefunctions, $|\psi_{nj}^k\rangle$. Here, the index k labels a set of random phases and jn the basis states. Choosing an arbitrary complete orthonormal basis set, $\{|\alpha\rangle\}$, and given that

$$\frac{1}{N} \sum_{k=1}^N e^{i(\theta_\alpha^k - \theta_\beta^k)} = \delta_{\alpha\beta}$$

for random phases θ_α^k , θ_β^k and N large, an expansion into random phase wavefunctions yields a representation of unity⁴³,

$$\begin{aligned} \mathbb{1} &= \frac{1}{N} \sum_{k=1}^N |\Psi^k\rangle \langle \Psi^k| = \frac{1}{N} \sum_{k=1}^N \sum_{\alpha\beta} e^{i(\theta_\alpha^k - \theta_\beta^k)} |\alpha\rangle \langle \beta| \\ &= \frac{1}{N} \sum_{k=1}^N \sum_{\alpha\beta} |\Psi_\alpha^k\rangle \langle \Psi_\beta^k|, \end{aligned} \quad (16)$$

where $|\Psi_\alpha^k\rangle = e^{i\theta_\alpha^k}|\alpha\rangle$ and $|\Psi^k\rangle = \sum_\alpha e^{i\theta_\alpha^k}|\alpha\rangle$. Identifying a set of suitable basis states $|\alpha\rangle$, only rovibrational states of the electronic ground state Hamiltonian $\hat{\mathbf{H}}_g$ need be considered since no electronic excitations are excited thermally. A separation of rotational and vibrational dynamics and subsequent expansion into partial waves is natural. Neglecting ro-vibrational couplings, the Hamiltonian for the vibrational motion is represented on an equidistant grid ($N_R = 1024$, $R_{min} = 3.0 a_0$, $R_{max} = 40.0 a_0$) for each partial wave J . In the following, we discuss three possible basis sets for the vibrational Hamiltonian, from which random phase functions, are generated. All three possibilities will lead when averaged to the initial thermal ensemble corresponding to the experiment. While formally equivalent, convergence of the thermal averages with respect to the number of required basis functions differs significantly for the three representations.

A. Grid-based random phase approach

The simplest but, as it turns out, most inefficient approach uses, for each partial wave J , the coordinate basis of δ -functions localized at each grid point, R , $\mathbb{1} = \sum_R |R, J\rangle\langle R, J|$.⁴³ A random phase wavefunction is obtained by multiplying each basis state with a different random phase, $\theta_{R,J}$,

$$|\Psi_{R,J}^k\rangle = e^{i\theta_{R,J}^k} |R, J\rangle,$$

where k labels one realization of random phases, $\{\theta_{R,J}^k\}$. The resulting wavefunction, $\langle R|\Psi_{R,J}^k\rangle$, has constant amplitude and a different random phase at each R . In this basis, the initial density operator is obtained by propagating each $|\Psi_{R,J}^k\rangle$ under $\hat{\mathbf{H}}_g^J = \hat{\mathbf{T}} + V_g(R) + \frac{J(J+1)}{2mR^2}$ in imaginary time, $\tau = i\frac{1}{2}\beta$. This yields $|\Psi_{R,J}^k\rangle_T = e^{-\frac{\beta}{2}\hat{\mathbf{H}}_g^J} |\Psi_{R,J}^k\rangle$ and thus the initial density operator,

$$\begin{aligned} \hat{\rho}_T(t=0) &= \frac{1}{Z} e^{-\frac{\beta}{2}\hat{\mathbf{H}}_g} e^{-\frac{\beta}{2}\hat{\mathbf{H}}_g} \frac{1}{N} \sum_{k=1}^N \sum_{R,J,R',J'} (2J+1)(2J'+1) e^{i(\theta_{R,J}^k - \theta_{R',J'}^k)} |R, J\rangle\langle R', J'| \\ &= \frac{1}{Z} \frac{1}{N} \sum_{k=1}^N e^{-\frac{\beta}{2}\hat{\mathbf{H}}_g} |\Psi_{R,J}^k\rangle\langle\Psi_{R,J}^k| e^{-\frac{\beta}{2}\hat{\mathbf{H}}_g}. \end{aligned}$$

A Chebychev propagator is employed for the imaginary time propagation⁴⁴ to obtain the N thermal random phase wavefunctions $|\Psi_{R,J}^k\rangle_T$ which represent the initial

states for the dynamics under the probe pulse. Thermally averaged time-dependent expectation values are obtained from Eq. (15), using cyclic permutations under the trace,

$$\begin{aligned} \text{Tr} [\hat{\mathbf{A}}\hat{\rho}_T(t)] &= \frac{1}{N} \sum_{k=1}^N \sum_{R,J} (2J+1)^2 \langle\Psi_{R,J}^k| \hat{\mathbf{A}}\hat{\mathbf{U}}(t,0) \hat{\rho}_T(t=0) \hat{\mathbf{U}}^\dagger(t,0) |\Psi_{R,J}^k\rangle \\ &= \frac{1}{Z} \frac{1}{N} \sum_{k=1}^N \sum_{R,J} (2J+1)^2 \langle\Psi_{R,J}^k| e^{-\frac{\beta}{2}\hat{\mathbf{H}}_g^J} \hat{\mathbf{U}}^\dagger(t,0) \hat{\mathbf{A}}\hat{\mathbf{U}}(t,0) e^{-\frac{\beta}{2}\hat{\mathbf{H}}_g^J} |\Psi_{R,J}^k\rangle \\ &= \frac{1}{N} \sum_{k=1}^N \sum_{R,J} (2J+1)^2 {}_T\langle\Psi_{R,J}^k(t)| \hat{\mathbf{A}} |\Psi_{R,J}^k(t)\rangle_T, \end{aligned} \quad (17)$$

where $|\Psi_{R,J}^k(t)\rangle_T = \hat{\mathbf{U}}(t,0) |\Psi_{R,J}^k\rangle_T$ are the propagated random-phase thermal wavefunctions. Note that while $|\Psi_{n,J}^k\rangle_T$ has zero components on all electronic states except the ground state, $|\Psi_{R,J}^k(t > 0)\rangle_T$ will be non-zero for all electronic states due to the interaction with the field. Typical expectation values are the excited state population after the pump pulse, possibly J -resolved. The corresponding operators are the projectors onto the elec-

tronically excited state, $\hat{\mathbf{P}}_e = |e\rangle\langle e|$ and $\hat{\mathbf{P}}_e^J$, i.e.,

$$Z\langle P_e^J(t_f)\rangle = \frac{1}{N} \sum_{k=1}^N \sum_R (2J+1)^2 |\langle e|\Psi_{R,J}^k(t_f)\rangle_T|^2.$$

The convergence of this approach is slow because there is no preselection of those basis states that are most relevant in the thermal ensemble.

B. Eigenfunction-based random phase approach

A preselection of the relevant states becomes possible by choosing the eigenbasis of H_g^J and evaluating the trace only for basis states with sufficiently large thermal weights, $e^{-\frac{\beta}{2}\hat{\mathbf{H}}_g^J} > \epsilon$. The eigenfunction-based random-phase wavefunctions are given by

$$|\Psi_{n,J}^k\rangle = e^{i\theta_{n,J}^k} |n, J\rangle,$$

$$\begin{aligned} \hat{\rho}_T(t=0) &= \frac{1}{Z} e^{-\frac{\beta}{2}\hat{\mathbf{H}}_g} e^{-\frac{\beta}{2}\hat{\mathbf{H}}_g} \frac{1}{N} \sum_{k=1}^N \sum_{n,J,n',J'} (2J+1)(2J'+1) e^{i(\theta_{n,J}^k - \theta_{n',J'}^k)} |n, J\rangle \langle n', J'| \\ &= \frac{1}{Z} \frac{1}{N} \sum_{k=1}^N \sum_{n,J,n',J'} (2J+1)(2J'+1) e^{-\frac{\beta}{2}E_{n,J} + i\theta_{n,J}^k} e^{-\frac{\beta}{2}E_{n',J'} - i\theta_{n',J'}^k} |n, J\rangle \langle n', J'|, \end{aligned} \quad (18)$$

where $E_{n,J}$ are the eigenvalues of the partial wave ground state Hamiltonian, $\hat{\mathbf{H}}_g^J$. Thermally averaged time-dependent expectation values are calculated analogously to Eq. (17),

$$\text{Tr} [\hat{\mathbf{A}} \hat{\rho}_T(t)] = \frac{1}{N} \sum_{k=1}^N \sum_{n,J} (2J+1)^2 {}_T \langle \Psi_{n,J}^k(t) | \hat{\mathbf{A}} | \Psi_{n,J}^k(t) \rangle_T, \quad (19)$$

where the time-dependent wavefunctions are the (real-time) propagated, Boltzmann-weighted eigenstates with random phases, $\theta_{n,J}^k$,

$$|\Psi_{n,J}^k(t)\rangle_T = \hat{\mathbf{U}}(t, 0) |\Psi_{n,J}^k\rangle_T = e^{-\frac{\beta}{2}E_{n,J} - i\theta_{n,J}^k} \hat{\mathbf{U}}(t, 0) |n, J\rangle.$$

The eigenfunction-based random phase approach requires diagonalization of the partial wave ground state Hamiltonians, $\hat{\mathbf{H}}_g^J$. Depending on the time required for the propagation of each basis state, this effort may very well be paid off by the much smaller number of basis states that need to be propagated.

C. Gaussian random phase wave packets / freely propagated random phase wavepackets

The third approach avoids diagonalization of the partial wave ground state Hamiltonians, $\hat{\mathbf{H}}_g^J$, approximating them by the kinetic energy, $\hat{\mathbf{T}}$, only. This approximation is valid at high temperatures where the kinetic energy of scattering atoms is much larger than their potential energy due to the interaction. It employs free thermal wavefunctions which are preselected according to their Boltz-

mann weight.⁴⁵ For each partial wave J , free thermal wavefunctions are obtained from δ -functions in momentum space, $\mathbb{1} = \sum_P |P, J\rangle \langle P, J|$, with a random phases, $\theta_{P,J}$,

$$|\Psi_{P,J}\rangle = e^{i\theta_{P,J}} |P, J\rangle.$$

Applying $e^{-\frac{\beta}{2}\hat{\mathbf{H}}_g^J} e^{i\theta_{P,J}^k} |P, J\rangle \approx e^{-\frac{\beta}{2}\frac{\mathbf{p}^2}{2m}} e^{i\theta_{P,J}^k} |P, J\rangle$ and Fourier transforming to coordinate space, thermal Gaussians, $|\Psi_G^{R_0}\rangle_T = e^{-\frac{(R-R_0)^2}{2\sigma_R^2}} |R, J\rangle$, are obtained. Their width is given by $\sigma_{R,T} = 1/\sigma_{P,T} = \sqrt{2m/\beta} = \sqrt{2mk_B T}$, i.e., it matches the Boltzmann distribution. The random phase, $\theta_{P,J}$, translates into the position of the Gaussian, R_0 . The density operator can thus be constructed from Gaussian functions in coordinate space by either positioning them at various points R_0 and averaging over R_0 , or propagating one Gaussian function with a single R_0 under $\hat{\mathbf{H}}_g^J$ for randomly chosen times, t_{prop}^k and averaging over those times. In the latter procedure, the probability amplitude of the two atoms is confined by the repulsive wall of the potential at shorter internuclear distances and an artificial reflecting barrier at long distance. The wavefunction then keeps on oscillating between the inner repulsive wall of the potential and the outer reflecting

barrier. The convergence of this method with respect to the photodissociation yield is initially very fast, only a few realizations are sufficient. The drawback of the procedure is that only the free part of the initial wavefunctions

is represented leaving out the interaction energy of the true scattering states. Averaging over propagation times, t_{prop}^k , thermal expectation values are obtained by

$$\text{Tr} [\hat{\mathbf{A}} \hat{\rho}_T(t)] = \frac{1}{N} \sum_{k=1}^N \sum_J (2J+1)^2 {}_T \langle \Psi_J^{t_{prop}^k}(t) | \hat{\mathbf{A}} | \Psi_J^{t_{prop}^k}(t) \rangle_T, \quad (20)$$

where $|\Psi_J^{t_{prop}^k}(t)\rangle_T = \hat{\mathbf{U}}(t,0)|\Psi_J^{t_{prop}^k}\rangle_T$ and $|\Psi_J^{t_{prop}^k}\rangle_T = e^{-i\hat{\mathbf{H}}_g^J t_{prop}^k} e^{-\frac{R^2}{2\sigma_{R,t}^2}} |R, J\rangle$.

IV. INTERACTION OF THE DIATOMS WITH PUMP AND PROBE PULSES

The interaction of the atom pair with the laser fields of the pump and probe pulses is simulated by solving time-dependent Schrödinger equations,

$$i\hbar \frac{\partial |\psi_{n,J}^k(t)\rangle}{\partial t} = \hat{\mathbf{H}}(t) |\psi_{n,J}^k(t)\rangle, \quad (21)$$

and thermally averaging the solutions. Absorption of the pump and probe pulses is considered separately neglecting coherent effects when pump and probe overlap in time which are unlikely to play any role here. The Hamiltonian describing the interaction of the diatom with the pump laser pulse is given by

$$\hat{\mathbf{H}}_{pump}^J(t) = \begin{pmatrix} \hat{\mathbf{H}}_{X^1\Sigma_g^+}^J & \chi^*(t, R) e^{-i\varphi(t)} & 0 & 0 \\ \chi(t, R) e^{i\varphi(t)} & \hat{\mathbf{H}}_{(1)^1\Pi_g}^J & W_1(R) & W_2(R) \\ 0 & W_1(R) & \hat{\mathbf{H}}_{(1)^3\Sigma_g}^J & W_3(R) \\ 0 & W_2(R) & W_3(R) & \hat{\mathbf{H}}_{(1)^3\Pi_g}^J \end{pmatrix}, \quad (22)$$

where $\hat{\mathbf{H}}_a^J + \omega_{g(e)}^S(t, \hat{\mathbf{R}})$ is the nuclear Hamiltonian of electronic state a ,

$$\hat{\mathbf{H}}_a^J = \hat{\mathbf{T}} + V_a(R) + \frac{J(J+1)}{2mR^2},$$

with $\hat{\mathbf{T}} = \hat{\mathbf{P}}^2/2m$ the vibrational kinetic energy, m the reduced mass, $V_a(R)$ the potential energy curve of electronic state a , and J the rotational quantum number. The two-photon coupling between the $X^1\Sigma_g^+$ (g) and $(1)^1\Pi_g$ (e) states is denoted by $\chi(t, R)$. The strong

laser field driving the two-photon transitions may lead to non-negligible dynamic Stark shifts in the $X^1\Sigma_g^+$ (g) and $(1)^1\Pi_g$ (e) states. $W_i(R)$ are the spin-orbit coupling matrix elements, cf. Eqs. (8)-(10).

The probe pulse promotes population from the $(1)^1\Pi_g$ excited state to the non-adiabatically coupled $(1)^1\Pi_u$ and $(2)^1\Pi_u$ states. Taking again the spin-orbit coupling of $(1)^1\Pi_g$ excited state to the $(1)^3\Sigma_g$ and $(1)^3\Pi_g$ states into account, the Hamiltonian describing the interaction of the photoassociated molecules with the probe pulse reads

$$\hat{\mathbf{H}}_{probe}^J(t) = \begin{pmatrix} \hat{\mathbf{H}}_{(1)^1\Pi_g}^J & E_{pr}(t)\mu_1(R) & E_{pr}(t)\mu_2(R) & W_1(R) & W_2(R) \\ E_{pr}(t)\mu_1(R) & \hat{\mathbf{H}}_{11}^J & V_{12}(R) & 0 & 0 \\ E_{pr}(t)\mu_2(R) & V_{12}(R) & \hat{\mathbf{H}}_{22}^J & 0 & 0 \\ W_1(R) & 0 & 0 & \hat{\mathbf{H}}_{(1)^3\Sigma_g}^J & W_3(R) \\ W_2(R) & 0 & 0 & W_3(R) & \hat{\mathbf{H}}_{(1)^3\Pi_g}^J \end{pmatrix}, \quad (23)$$

where $\mu_{1/2}(R)$ are the transition dipole moments between the $(1)^1\Pi_g$ state and the $^1\Pi_u$ states, $\hat{\mathbf{H}}_{ii}^J = \hat{\mathbf{T}} + V_{ii}^d(R) +$

$\frac{J(J+1)}{2mR^2}$, $i = 1$ or 2 , where $V_{ii}^d(R)$ is the diagonal diabatic

potential, cf. Eq. (1). $V_{12}(R)$ is the coupling between the $^1\Pi_u(1)$ and $^1\Pi_u(2)$ states in the diabatic representation, and $E_{pr}(t)$ denotes the electric field of the probe laser pulse.

The photoassociation is studied numerically by solving the time-dependent Schrödinger equations, Eq. (21), for the Hamiltonian $\hat{\mathbf{H}}_{pump}$, Eq. (22), with a Chebychev propagator.⁴⁶ The pump laser pulse excites a small portion of the incoherent ensemble of ground state atom pairs. This action corresponds to a filtering and might

thus lead to higher purity and coherence of the photoassociated molecules. In order to study the excited state purity,

$$\mathcal{P}_e(t) = \text{Tr}[\hat{\rho}_{T,e}^2(t)], \quad (24)$$

and the dynamical coherence measure, $\mathcal{C}_e(t)$, we construct the normalized density operator of electronic state e , $\hat{\rho}_{T,e}(t)$,

$$\hat{\rho}_{T,e}(t) = \frac{1}{\langle P_e(t) \rangle} \frac{1}{N} \sum_{k=1}^N \sum_{n,J,n',J'} (2J+1)(2J'+1) \hat{\mathbf{P}}_e |\Psi_{n,J}^k(t)\rangle_T \langle \Psi_{n',J'}^k(t)| \hat{\mathbf{P}}_e.$$

In the grid representation using N_R grid points, this becomes a matrix of size $N_R \times N_R$,

$$\rho_{T,e}(R, R'; t) = \frac{1}{\langle P_e(t) \rangle} \frac{1}{N} \sum_{k=1}^N \sum_{n,J,n',J'} (2J+1)(2J'+1) \Psi_{T,n,J}^{k,e}(R, t) \Psi_{T,n',J'}^{k,e*}(R', t),$$

where $\Psi_{T,n,J}^{k,e}(R, t) = \langle R, e | \Psi_{n,J}^k(t) \rangle_T$ is the excited state projection of the propagated k th thermal random phase wavefunction. Since we expect to populate only a limited number of excited state eigenfunctions, say N_m , it is computationally advantageous to transform the excited state component of the propagated thermal wavefunctions into

the eigenbasis of the electronically excited state,

$$\Psi_{T,n,J}^{k,e}(R, t) = \sum_m c_m^{k,n,J}(t) \varphi_{e,m}(R),$$

with

$$c_m^{k,n,J}(t) = \int \Psi_{T,n,J}^{k,e}(R, t) \varphi_{e,m}^*(R) dR.$$

The resulting density matrix,

$$\rho_{T,e}^{m,m'}(t) = \frac{1}{\langle P_e(t) \rangle} \frac{1}{N} \sum_{k=1}^N \sum_{n,J,n',J'} (2J+1)(2J'+1) c_m^{k,n,J}(t) c_{m'}^{k,n',J'}(t),$$

is only of size $N_m \times N_m$ and can more efficiently be squared. Moreover, it lends itself naturally to the evaluation of the dynamical coherence measure. In the eigenbasis, we can easily decompose the density operator into its static (diagonal) and dynamic (off-diagonal) part, $\hat{\rho} = \hat{\rho}_{stat} + \hat{\rho}_{dyn}$. Such a decomposition has been motivated in the study of dissipative processes, in particular by the fact that pure dephasing does not alter the static part.^{47,48} The dynamical coherence measure,

$$\mathcal{C}_e(t) = \text{Tr}[\hat{\rho}_{T,e,dyn}^2(t)], \quad (25)$$

captures the part of the purity that arises from the dynamical part of the density operator.^{47,48}

V. CONVERGENCE OF THE THERMAL AVERAGING PROCEDURES: PHOTOASSOCIATION PROBABILITY

The convergence with respect to the number of random phase realizations, N , is checked with respect to Boltzmann weighting as follows. Each random phase wave function, $|\Psi_{R,J}^k\rangle_T$, $|\Psi_{n,J}^k\rangle_T$, or $|\Psi_J^{t^{prop},k}\rangle_T$, is projected onto the eigenstates, $|n, J\rangle$, of the electronic ground state. The resulting overlaps are averaged over all possible realizations, k ,

$$C_{T,n,J}^N = \frac{1}{N} \sum_{k=1}^N \langle n, J | \Psi_{\alpha}^k \rangle_T. \quad (26)$$

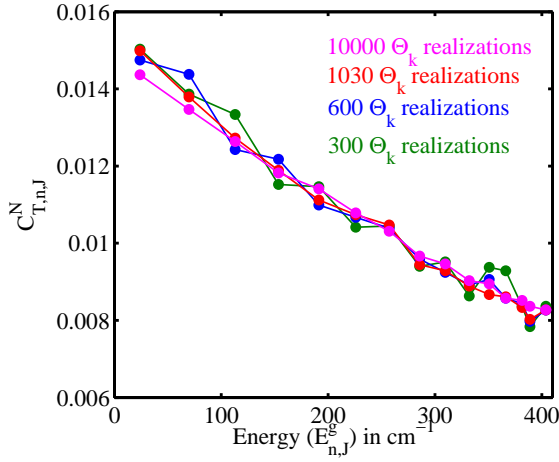


FIG. 2. Logarithm of the overlaps $C_{T,n,J}^N$, cf. Eq. (26), vs energy, $E_{n,J}^g$ ($J=0$) for the grid-based random phase approach.

Plotting the overlap, $C_{T,n,J}^N$ versus eigenenergy, $E_{n,J}^g$, of the electronic ground state Hamiltonian, \hat{H}_g^J , yields oscillations around a straight line, see Fig. 2. The slope multiplied by the Boltzmann constant represents the inverse temperature, $\frac{1}{T}$. Convergence is defined by approaching this line. A perfect straight line means that a temperature can reliably be extracted from our numerical representation of the thermal ensemble. Decreasing oscillations around a straight line indicate that the temperature estimated from the thermally averaged overlaps is close to the actual temperature of the experiment.

For the grid based random phase approach, cf. section III A, the number of realizations, N , required to reach convergence was found to be much larger than the number of grid points $N_R = 1024$. As the number of realizations, N , is increased, the oscillations around the straight line decrease in Fig. 2. Note that for the eigenfunction-based random phase approach this consistency check with respect to temperature will give a straight line by construction. The free propagation approach will approximate tightly the Boltzmann weighting of the scattering states.

The initial thermal density of atom pairs, cf. Eq. (18), is shown as a function of interatomic distance in Fig. 3 for the eigenfunction based random phase approach. For photoassociation, distances smaller than $\sim 15 a_0$ are relevant. The thermal density is converged in this region by including rotational quantum numbers up to $J = 200$. The contribution of higher partial waves only ensures a constant density at large interatomic distances, see insert of Fig. 3. The long-distance part naturally converges very slowly but this is irrelevant for the dynamical calculations. The peak at short interatomic separations is due to bound levels, shape resonances and the classical turning point of the scattering states at the repulsive barrier of the potential: The difference between the black and yellow curves in Fig. 3 indicates the contribution of

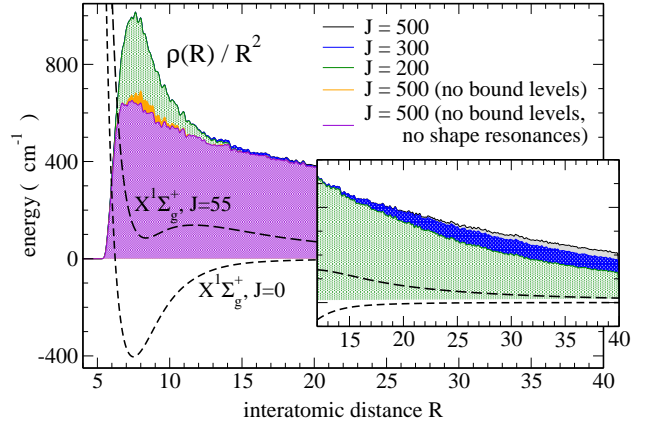


FIG. 3. Initial thermal density $\rho_{T,g}(R)/R^2$ of ground state atom pairs calculated with the eigenfunction-based random phase approach (using 200 realizations for each J).

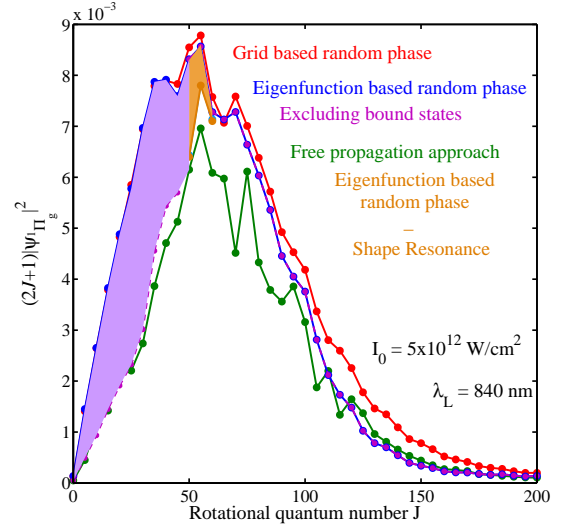


FIG. 4. Population transferred to $^1\Pi_g$ state by the pump pulse, for different initial partial waves J , averaged over random phase wavefunctions (number of realizations: 200 for the 200 lowest eigenfunctions, 1030 in the grid-based random phase approach and 17 in the free propagation approach). The shaded part shows the contribution of bound levels in the eigenfunction based approach. The orange shaded part shows the contributions of the shape resonances. The statistical errors in these curves are estimated as $\sigma/\text{mean} \sim 0.11$ for the eigenvalue approach, $\sigma/\text{mean} \sim 0.09$ for the grid-based approach and $\sigma/\text{mean} \sim 0.26$ for the free propagation approach.

bound levels, the difference between the yellow and the purple curve that of shape resonances.

The population transferred from the initial incoherent ensemble to the $^1\Pi_g$ state by the pump pulse is shown in Figure 4, comparing the grid-based, eigenfunction-based and free propagation based random phase approach. The

thermal averaging procedure has been repeated for increasing initial rotational quantum number, J . That is, for each rotational barrier, grid-based, eigenfunction-based and Gaussian random phase wave functions are propagated in real time with the full, time-dependent Hamiltonian, \hat{H}_{pump}^J . Expectation values, such as the population of the $^1\Pi_g$ state after the pump pulse is over, are calculated for each random phase realization, k , or propagation time, t_{prop} , respectively, and averaged over, including the rotational degeneracy factor $J+1$, cf. Eqs. (17), (19), and (20). The three approaches qualitatively give the same result with a steep rise at low J -values, a peak at $J = 55$ and an exponential tail for $J \geq 120$. Each random phase approach represents a statistical sampling of the photoassociation yield. For small N the free propagation approach converged extremely fast. For refined results more sampling is required. The deviation of an expectation value from its mean scales as $1/\sqrt{N}$ where N is the number of realizations. This was checked for $J = 55$ and $J = 100$ the pre-factor $\sigma/mean = \bar{s}/\sqrt{N}$ is estimated as $\bar{s} \sim 0.37$ for the free propagation method $\bar{s} \sim 0.17$ for the eigenvalue method and $s \sim 0.30$ for the grid based method. This makes the eigenvalue method converge fastest for large N .

For low partial waves, the grid based (red curve) and the eigenfunction based (blue curve) random phase approaches agree very well with each other. Once the bound levels are removed from the eigenfunction based approach (dashed purple curve), the eigenfunction-based approach agrees with the free propagation approach (green curve). This comparison allows for estimating the contribution of the bound levels. For $J \geq 50$ the ground state potential does not support any bound levels due to the high centrifugal barrier. The total contribution of the bound part of the spectrum to the excitation of $^1\Pi_g$ population amounts to about 15%. The free propagation approach does not account for the bound part since it builds a Boltzmann ensemble in the asymptotic, flat part of the potential, based on kinetic energy only. Relatively large deviations between the free propagation approach and the other methods are also observed for $50 \leq J \leq 65$. This is partially attributed to shape resonances residing behind the centrifugal barrier. Due to the finite propagation time ($t_{prop} = 150$ ps) in the free propagation method, only those resonances are captured that have a lifetime that is shorter than t_{prop} . The contribution of long-lived shape resonances is absent since these resonances are not sampled by the free propagation approach. When the contributions of the shape resonances are added to the free propagation method (cyan curve) some of the discrepancy is removed. The differences between $J = 60$ to $J = 90$ are attributed to insufficient sampling of the free propagation method (only 17 realizations). At large J , the grid based random phase approach overestimates the exponential tail. This can be rationalized in terms of a biased sampling with too many points dedicated to high energies on the repulsive part of the centrifugal barrier.

The role of shape resonances is further analyzed in

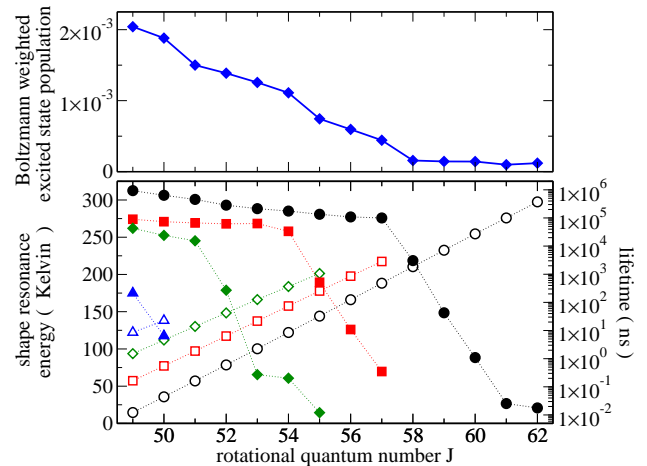


FIG. 5. Top panel: Population photoassociated out of shape resonances vs initial partial wave J . Bottom panel: Position in Kelvin (empty symbols) and lifetimes in nanoseconds (filled symbols) of the shape resonances vs partial wave J .

Fig. 5 which displays the total photoassociation yield that originates from shape resonances (top panel) as well as the positions and lifetimes of the shape resonances (bottom panel). The shape resonances were calculated using a complex absorbing potential.⁴⁹ Diagonalization of the non-Hermitian Hamiltonian was followed by propagation under the ground state Hamiltonian to get sufficiently accurate lifetimes. Shape resonances are found for $J = 49, \dots, 62$. For $J = 49, 50$, four shape resonances reside behind the centrifugal barrier, for $J = 51, \dots, 55$ three, for $J = 56, 57$ two and for $J = 58, \dots, 62$ one. The positions of the resonances lie between 15 K and 300 K and scale linearly with the rotational quantum number J (left-hand y-axis of the bottom panel of Fig. 5). The lifetimes scale step-wise exponentially with J (and thus with energy) with the lowest-lying resonances having the longest lifetimes. Exponential scaling is expected if the lifetime is caused by tunneling out of the rotational barrier alone. The multi-exponential scaling can be attributed to the appearance of further resonances with the same rotational quantum number. For $J = 49 \dots, 57$, i.e., for those partial waves where very long-lived resonances are observed, the contribution of the shape resonances to the photoassociation yield is fairly significant. It amounts to 23% for $J = 50$ and 9% for $J = 55$. This is not surprising since shape resonances represent quasi-bound states that are ideally suited for photoassociation. They give structure to the continuum of scattering states which otherwise is completely flat at high temperature. This can be utilized for generation of coherence and control.

The missing contribution of photoassociation out of shape resonances in the free propagation approach explains the discrepancy with the eigenfunction based method for the photoassociation yield in Fig. 4. If the

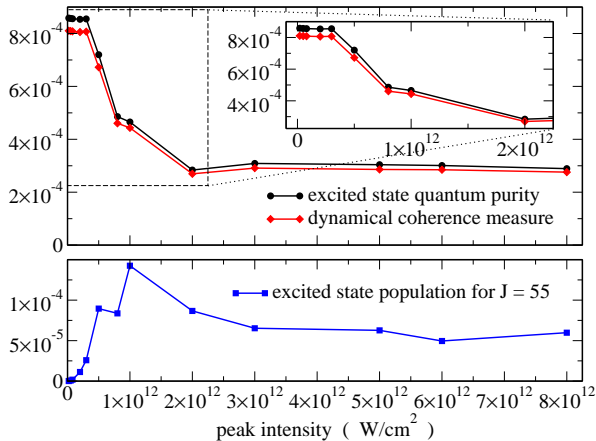


FIG. 6. Top panel: Excited state purity, $\mathcal{P}_e(t_{final})$, and coherence measure, $\mathcal{C}_e(t_{final})$, cf. Eqs. (24) and (25), vs pulse intensity for the subensemble of photoassociated molecules. Bottom panel: Photoassociation yield for $J = 55$ as a function of peak pulse intensity.

contribution of shape resonances to the photoassociation yield is subtracted from the result of the eigenfunction based approach, the remaining error of 3% for $J = 50$ and 10% for $J = 55$ is easily rationalized in terms of the statistical sampling.

In conclusion, the free propagation approach is numerically most efficient method for a rough estimate. When further refinement is required the eigenvalue approach converges faster by a factor of 2. The free propagation approach excludes the bound part of the spectrum and the resonances, it comes with error bars of about 15%. If more accurate results are desired, the eigenfunction based random phase approach is the method of choice. The eigenfunction based method is also best suited to capture the contribution of bound states and shape resonances to the photoassociation yield.

VI. INTERPLAY OF COHERENCE AND PHOTOASSOCIATION YIELD

In order to rationalize and quantify the generation of the coherence, that is observed experimentally^{28,29}, out of a completely incoherent initial ensemble, we consider the change in quantum purity, $\text{Tr}[\hat{\rho}^2]$, due to the femtosecond laser pulses. The initial purity, determined by the temperature, $T = 1000\text{ K}$, and density, $\rho = 4.8 \cdot 10^{16}\text{ atoms/cm}^3$, of the experiment, is estimated in terms of the purity of a single atom pair represented in our computation and the probability, p_2 , of finding two atoms in our computation volume, \mathcal{V} . Given ρ and $\mathcal{V} = 4/3\pi r^3 = 6.33 \cdot 10^{-21}\text{ cm}^3$, we find $p_2 = 9.2 \cdot 10^{-8}$. The purity of a single atom pair in our computation box is given by the vibrational purity weighted by the probability, P_J , for occupation of the sub-ensemble with angu-

lar momentum J . For an atom pair in their electronic ground state, the purity becomes $\mathcal{P}^g = p_2^2 \sum_J P_J^2 \mathcal{P}_J^g$ where $\mathcal{P}_J^g = \text{Tr}[(e^{-\beta \hat{\mathbf{H}}_g^J})^2]/Z_J^2$, and $\hat{\mathbf{H}}_g^J$ and Z_J are the Hamiltonian for vibrational motion and partition function, respectively, of partial wave J . Evaluating \mathcal{P}_J^g with freely propagated thermal random-phase wavefunctions, we obtain $\mathcal{P}^g = 2.6 \cdot 10^{-20}$ for the initial purity. While the effect of bound levels and shape resonances is not accounted for by the free propagation approach, their contribution to the initial purity is negligible. This is due to the fact that random phase wavefunctions for partial waves up to $J = 800$ need to be considered to obtain converged results. The bound levels and shape resonances occur for small bands of J . Their weight within the large ensemble consisting of 800 partial waves is correspondingly small. For the ensemble of molecules in the electronically excited $^1\Pi_g$ state, the density operator is given by $\hat{\rho}^e = \sum_J P_J^e \hat{\rho}_J^e$. Here, P_J^e is the probability for occupation of the excited state sub-ensemble with angular momentum, J , cf. Fig. 4. $\hat{\rho}_J^e$ is the normalized density operator of the excited state J sub-ensemble which is constructed by incoherently averaging dyadic products of the propagated thermal wavefunctions, $|\psi_{n,J}(t_{final})\rangle\langle\psi_{n,J}(t_{final})|$, over all random phases n and partial waves J (t_{final} denotes the time when the pump pulse is over). The purity for the excited state sub-ensemble is then given by $\mathcal{P}^e = \sum_J (P_J^e)^2 \text{Tr}[(\hat{\rho}_J^e)^2]$. We obtain a purity $\mathcal{P}^e = 3.04 \cdot 10^{-4}$ for the molecular sub-ensemble in the $^1\Pi_g$ excited state for the experimental pulse parameters. We thus observe a dramatic increase in the quantum purity, $\text{Tr}[\hat{\rho}^2]$, induced by the femtosecond laser pulse. The underlying physical mechanism can be viewed as "Franck-Condon filtering": for a given initial J value there is only a limited range of collision energies that allow the colliding pair to reach the Franck-Condon window for PA located at short internuclear distances¹¹.

In order to obtain a quantitative estimate of the degree of distillation achieved by the fs-PA process, we have calculated the purity of ensemble of photoassociated molecules in the $^1\Pi_g$ state for a range of laser intensities, cf. Fig. 6. For weak fields, the purity is roughly constant as a function of intensity and almost three times larger than the purity obtained for the intensity of $5 \times 10^{12}\text{ W/cm}^2$ used in the experiment. As intensity is increased, a sudden drop in the purity is observed which levels off at large intensities. We attribute this drop to power broadening for strong fields, which brings more atom pairs into the Franck-Condon window for PA. The purity increase with respect to the initial ensemble is nevertheless many orders of magnitude for both weak and strong field. To further analyze the generation of quantum coherence, it is possible to separate static and dynamic contributions, $\hat{\rho} = \hat{\rho}_{stat} + \hat{\rho}_{dyn}$. This is most easily achieved in the energy representation where the static (dynamic) part corresponds to the diagonal (off-diagonal) matrix elements. The dynamical contributions are quantified by the coherence measure $\mathcal{C} = \text{Tr}[\hat{\rho}_{dyn}^2(t)]$ ⁴⁷. Tracing the coherence measure of the

excited state, C^e , as a function of laser intensity (red diamonds in Fig. 6) shows that most of the purity comes from the dynamical contribution ($C^e = 2.86 \cdot 10^{-4}$ for the experimental intensity of $5 \times 10^{12} \text{ W/cm}^2$).

VII. CONCLUSIONS

We have described two-photon femtosecond photoassociation of magnesium atoms from first principles using state of the art *ab initio* methods and quantum dynamical calculations. Highly accurate potential energy curves were obtained using the coupled cluster method and a large basis set. Two-photon couplings and dynamic Stark shifts are important to correctly model the interaction of the atom pairs with the strong field of a femtosecond laser pulse. They were calculated within the framework of the equation of motion (linear response) coupled cluster method. The photoassociation dynamics were obtained by solving the Schrödinger equation for all relevant partial waves, accounting for the laser-matter interaction in a non-perturbative way.

An efficient numerical method has been developed to describe the incoherent thermal ensemble that is the initial state for photoassociation at high temperatures. It is based on random phase wave packets which can be built from eigenfunctions of the grid, the Hamiltonian, or the kinetic energy. The latter can supply a rough estimate with ~ 17 realizations. This approach yields qualitatively correct results. It neglects, however, the contribution from bound levels and long-lived shape resonances and therefore comes with error bars of about 15%. The best compromise between high accuracy and convergence is found for the eigenfunction-based method where random phase realizations are built from the eigenfunctions of the electronic ground state Hamiltonian. About 200 partial waves and 200 realizations for each partial wave are required for converged photoassociation dynamics. Time-dependent thermal averages are obtained by propagating each of the random phase basisfunctions and incoherently summing up all single expectation values.

The random phase approach allows for constructing the thermal atom pair density as a function of interatomic separation for high temperatures. This is important to highlight the difference between hot and cold photoassociation^{42,45,50}. In the cold regime, the largest density is defined by the quantum reflection and resides in the long-distance, downhill part of the potential. The opposite is true in the hot regime: Here, the largest density is found in the repulsive part of the ground state potential. This is due to the many partial waves that are thermally populated and the colliding atom pairs having sufficiently high kinetic energy to overcome the rotational barriers. For specific partial waves, shape resonances are found to be important. This is not surprising since they represent quasi-bound states that are ideally suited for photoassociation. At very low temperatures, most partial waves are frozen out and the scattering is almost

exclusively *s*-wave. The role of the rotational quantum numbers J is less important in the electronically excited state but it is still detectable in form of quantum beats.²⁸ Both hot and cold photoassociation come with advantages as well as drawbacks. In the hot regime, molecules with much shorter bond length than in the cold regime are formed. However, the quantum purity and coherence of the created molecules is much larger in the cold regime where dynamical correlations exist prior to photoassociation. These correlations indicate pre-entanglement of the atom pair. Making a molecule corresponds to entangling two atoms, and photoassociation amounts to filtering out and entangled subensemble both in the hot and cold regime.

Our study has opened up the possibility to study femtosecond photoassociation and its control at high temperatures and to investigate systematically the generation of coherence out of an incoherent initial state. Future work will address the efficient theoretical description of the probe step.

ACKNOWLEDGMENTS

This study was supported by the Israeli Science Foundation ISF Grant No. 1450/10. RM and MT would like to thank the Polish Ministry of Science and Higher Education for the financial support through the project N N204 215539. MT was supported by the project operated within the Foundation for Polish Science MPD Programme co-financed by the EU European Regional Development Fund. Financial support from the Deutsche Forschungsgemeinschaft through the Emmy Noether programme and Sfb 450 is gratefully acknowledged.

- ¹R. Kosloff, S. Rice, P. Gaspard, S. Tersigni, and D. Tannor, *Chem. Phys.* **139**, 201 (1989).
- ²S. A. Rice and M. Zhao, *Optical control of molecular dynamics* (John Wiley & Sons, 2000).
- ³P. Brumer and M. Shapiro, *Principles and Applications of the Quantum Control of Molecular Processes* (Wiley Interscience, 2003).
- ⁴D. J. Tannor, *Introduction to Quantum Mechanics: A time-dependent perspective* (Palgrave Macmillan, 2007).
- ⁵R. J. Gordon and S. A. Rice, *Annu. Rev. Phys. Chem.* **48**, 601 (1997).
- ⁶T. Brixner and G. Gerber, *ChemPhysChem* **4**, 418 (2003).
- ⁷M. Dantus and V. V. Lozovoy, *Chem. Rev.* **104**, 1813 (2004).
- ⁸M. Wollenhaupt, V. Engel, and T. Baumert, *Annu. Rev. Phys. Chem.* **56**, 25 (2005).
- ⁹O. Kühn and L. Wöste, eds., *Analysis and control of ultrafast photoinduced reactions* (Springer, Berlin, 2007).
- ¹⁰U. Marvet and M. Dantus, *Chem. Phys. Lett.* **245**, 393 (1995).
- ¹¹P. Backhaus and B. Schmidt, *Chem. Phys.* **217**, 131 (1997).
- ¹²P. Gross and M. Dantus, *J. Chem. Phys.* **106**, 8013 (1997).
- ¹³P. Backhaus, J. Manz, and B. Schmidt, *J. Phys. Chem. A* **102**, 4118 (1998).
- ¹⁴P. Backhaus, B. Schmidt, and M. Dantus, *Chem. Phys. Lett.* **306**, 18 (1999).
- ¹⁵R. de Vivie-Riedle, K. Sundermann, and M. Motzkus, *Faraday Discuss.* **113**, 303 (1999).
- ¹⁶M. Bonn, S. Funk, C. Hess, D. N. Denzler, C. Stampfl, M. Schefler, M. Wolf, and G. Ertl, *Science* **285**, 1042 (1999).

- ¹⁷D. Geppert, A. Hofmann, and R. de Vivie-Riedle, *J. Chem. Phys.* **119**, 5901 (2003).
- ¹⁸P. Nuernberger, D. Wolpert, H. Weiss, and G. Gerber, *Proc. Natl. Acad. Sci. USA* **107**, 10366 (2010).
- ¹⁹V. Zeman, M. Shapiro, and P. Brumer, *Phys. Rev. Lett.* **92**, 133204 (2004).
- ²⁰K. M. Jones, E. Tiessinga, P. D. Lett, and P. S. Julienne, *Rev. Mod. Phys.* **78**, 483 (2006).
- ²¹C. P. Koch and R. Kosloff, *Phys. Rev. Lett.* **103**, 260401 (2009).
- ²²P. Pellegrini, M. Gacesa, and R. Côté, *Phys. Rev. Lett.* **101**, 053201 (2008).
- ²³S. V. Alyabyshev and R. V. Krems, *Phys. Rev. A* **82**, 030702 (2010).
- ²⁴R. Aĝanoĝlu, M. Lemeshko, B. Friedrich, R. González-Férez, and C. P. Koch, “Controlling a diatomic shape resonance with non-resonant light,” *arXiv:1105.0761* (2011).
- ²⁵W. Salzmann, T. Mullins, J. Eng, M. Albert, R. Wester, M. Weidemüller, A. Merli, S. M. Weber, F. Sauer, M. Plewicky, F. Weise, L. Wöste, and A. Lindinger, *Phys. Rev. Lett.* **100**, 233003 (2008).
- ²⁶A. Merli, F. Eimer, F. Weise, A. Lindinger, W. Salzmann, T. Mullins, S. Götz, R. Wester, M. Weidemüller, R. Aĝanoĝlu, and C. P. Koch, *Phys. Rev. A* **80**, 063417 (2009).
- ²⁷C. P. Koch, E. Luc-Koenig, and F. Masnou-Seeuws, *Phys. Rev. A* **73**, 033408 (2006).
- ²⁸L. Rybak, S. Amaran, L. Levin, M. Tomza, R. Moszynski, R. Kosloff, C. P. Koch, and Z. Amitay, *Phys. Rev. Lett.* (2011).
- ²⁹L. Rybak, Z. Amitay, S. Amaran, R. Kosloff, M. Tomza, R. Moszynski, and C. P. Koch, *Faraday Discuss.* **153**, 383 (2011).
- ³⁰Y. Silberberg, *Annu. Rev. Phys. Chem.* **60** (2009).
- ³¹S. F. Boys and F. Bernardi, *Mol. Phys.* **19**, 553 (1970).
- ³²W. J. Balfour and A. E. Douglas, *Can. J. Phys.* **48**, 901 (1970).
- ³³W. Skomorowski, M. Tomza, and R. Moszynski, in preparation.
- ³⁴J. Olsen and P. Jørgensen, *J. Chem. Phys.* **82**, 3235 (1985).
- ³⁵C. Hättig, O. Christiansen, and P. Jørgensen, *J. Chem. Phys.* **108**, 8331 (1998).
- ³⁶C. Hättig, O. Christiansen, and P. Jørgensen, *J. Chem. Phys.* **108**, 8355 (1998).
- ³⁷O. Christiansen, A. Halkier, H. Koch, P. Jørgensen, and T. Helgaker, *J. Chem. Phys.* **108**, 2801 (1998).
- ³⁸C. Hättig, O. Christiansen, S. Coriani, and P. Jørgensen, *J. Chem. Phys.* **109**, 9237 (1998).
- ³⁹C. Hättig, O. Christiansen, and J. Gauss, *J. Chem. Phys.* **109**, 4745 (1998).
- ⁴⁰DALTON, a molecular electronic structure program, Release 1.2 (2001), see <http://www.kjemi.uio.no/software/dalton/dalton.html>.
- ⁴¹MOLPRO is a package of *ab initio* programs written by H.-J. Werner and P. J. Knowles and with contributions from R. D. Amos, A. Bernhardsson, A. Berning, P. Celani, D. L. Cooper, and M. J. O. Deegan, A. J. Dobbyn, F. Eckert, C. Hampel, G. Hetzer, T. Korona, R. Lindh, A. W. Lloyd, S. J. McNicholas, F. R. Manby, W. Meyer, M. E. Mura, A. Nicklass, P. Palmieri, R. Pitzer, G. Rauhut, M. Schütz, H. Stoll, A. J. Stone, R. Tarroni, and T. Thorsteinsson.
- ⁴²C. P. Koch, R. Kosloff, E. Luc-Koenig, F. Masnou-Seeuws, and A. Crubellier, *J. Phys. B* **39**, S1017 (2006).
- ⁴³D. Gelman and R. Kosloff, *Chem. Phys. Lett.* **381**, 129 (2003).
- ⁴⁴R. Kosloff and H. Tal-Ezer, *Chem. Phys. Lett.* **127**, 223 (1986).
- ⁴⁵J. Vala, O. Dulieu, F. Masnou-Seeuws, P. Pillet, and R. Kosloff, *Phys. Rev. A* **63**, 013412 (2001).
- ⁴⁶R. Kosloff, *Annu. Rev. Phys. Chem.* **45**, 145 (1994).
- ⁴⁷U. Banin, A. Bartana, S. Ruhman, and R. Kosloff, *J. Chem. Phys.* **101**, 8461 (1994).
- ⁴⁸U. Banin, R. Kosloff, and S. Ruhman, *Chem. Phys.* **183**, 289 (1994).
- ⁴⁹Nimrod and Moiseyev, *Physics Reports* **302**, 212 (1998).
- ⁵⁰A. Vardi, D. Abrashkevich, E. Frishman, and M. Shapiro, *J. Chem. Phys.* **107**, 6166 (1997).